Proceedings of the 8th International Conference on Gas Hydrates (ICGH8-2014),
Beijing, China, 28 July - 1 August, 2014

HOW METHANE SOLUBILITY CHANGES WITH HYDRATE SATURATION, PORE SIZE AND SALT CONTENT IN POLYDISPERSED MEDIA

Julia T. Irizarry* **and Alan W. Rempel**
Department of Geological Sciences, University of Oregon
Eugene, OR 97403-1272, USA

ABSTRACT

The controls on pore-scale hydrate distribution must be evaluated in order to better characterize the quality, volume, and potential hazard of methane hydrate deposits. Surface energy and wetting effects influence solidification behavior in porous media. In the two-phase hydrate-liquid stability zone, the solubility of methane at the onset of hydrate formation increases as the pore size decreases and causes hydrate crystals to occupy smaller volumes with larger surface curvatures. Two-dimensional models of methane solubility demonstrate how changes in crystal-liquid interface geometry take place as the hydrate saturation level increases. These interface changes cause the methane solubility to increase further. Similar behavior is responsible for the dependence of ice saturation on temperature in porous media, and between gas saturation and matrix potential in the vadose zone. Here, we describe our algorithm for assembling a three-dimensional porous medium from a particle size distribution that can be specified to match laboratory or field constraints. We outline how Monte Carlo integration techniques can be used to predict changes in methane solubility with hydrate saturation in such polydispersed porous media. The effects of surface energy are generally expected to dominate until a threshold in hydrate saturation is reached, beyond which wetting effects are responsible for most of the residual liquid with its dissolved contents. Variations in solubility with pore geometry, hydrate saturation, and salt content offer powerful constraints on the deposition of hydrates and especially on the development of anomalies. Ongoing work is focused on the implications of our results for explaining behavior observed in boreholes and inferred from geophysical data.

Keywords: gas hydrates, heterogeneous medium, premelting, wetting dynamics

NOMENCLATURE

c Concentration at given saturation level [m^3/m^3]
c_B Bulk concentration [m^3/m^3]
c_{eq} Equilibrium solubility of hydrate guest [kg/kg]
c_3 Solubility of hydrate guest in 3-phase equilibrium at temperature T_3 [kg/kg]
d thickness of liquid film [m]
L Latent heat of fusion [J/kg]
n Number of particles
P_0 Disjoining pressure [Pa]
P_T Strength of wetting interactions [Pa]
R Radius of adjacent particle [m]
R_h Radius of curvature for hydrate [m]
S_l Liquid fraction [m^3/m^3]
T Temperature [K]
T_m Reference equilibrium temperature [K]
T_{m0} Melting temperature of the pure system [K]
T_3 Temperature for 3-phase equilibrium at concentration c_3 [K]
x Horizontal distance coordinate [m]
y Horizontal distance coordinate [m]
z Vertical distance coordinate [m]
α Temperature scale in solubility relation [K]
β Exponent in the power law
Γ Liquidus slope
Δc_{eq} Change in methane solubility [kg/kg]
λ Film thickness [m]
κ Curvature of the phase boundary [m^{-1}]
ρ_g Hydrate density [kg/m^3]
ρ_h Hydrate density [kg/m^3]
Φ Porosity [m^2/m^2]
γ_{sl} Surface energy [J/m^2]

*Corresponding author: Phone: +1 910 723 7703 E-mail: juliai@uoregon.edu

INTRODUCTION

The sophistication of efforts to understand the global hydrate reservoir volume and distribution continue to mature. Economic and environmental factors driving these developments include the propensity of gas hydrates to accumulate in deep-sea pipelines (flow assurance problems) [1], their ability to increase the likelihood for offshore sediment failure and landslides [2], their increasing viability as a "clean" energy resource [3], and their potential capacity to act as a powerful source of greenhouse gases [4].

Although efforts to determine the total volume of global hydrate reservoirs remain a prominent research goal [5], concentrated hydrate anomalies are increasingly recognized for their disproportionate importance to the economic and environmental issues that drive hydrate research [3]. The formation and behavior of these anomalies cannot be described without understanding the micro scale effects and interactions between the hydrate and the surrounding porous media that determine whether methane precipitates to form hydrate or remains dissolved in solution. This study considers the influence of surface energy and wetting interactions on the solubility of methane in a model porous medium. We build upon the successful results of similar efforts that describe the residual liquid saturation in partially frozen sediments below the bulk melting temperature [6].

HYDRATE GEOMETRY AND SOLUBILITY

Our immediate goal is to expand upon the results of previous 2-D calculations [7] and determine how micro scale effects perturb the methane solubility in more realistic 3-D particle packing. The change in chemical potential imposed by surface energy and wetting effects can be expressed in terms of the deviation from a reference equilibrium temperature T_m. In the absence of impurities we have that

$$\frac{\rho_h L}{T_m}\left(T_m - T\right) = \gamma_{hl}\kappa + P_0\left(\frac{\lambda}{d}\right)^{\beta}, \qquad (1)$$

where all symbols are defined in the nomenclature above, with surface energy effects proportional to the curvature κ and wetting effects approximated using a power law in film thickness d. This offset to the chemical potential modifies the phase behavior so that the equilibrium solubility can be written as

$$C_{eq} \approx c_3 \exp\left(\frac{T_m - T_3}{\alpha}\right) \approx c_3\left(1 + \frac{T_m - T}{\alpha}\right)\exp\left(\frac{T - T_3}{\alpha}\right), \qquad (2)$$

where the approximation is valid as long as $T_m - T \ll \alpha$, which is true for most cases of interest. The fractional change in methane solubility Δc_{eq} defined by the difference between solubility in the pore space and bulk solubility, normalized by the bulk solubility is

$$\Delta c_{eq} = \exp\left(\frac{T_m - T}{\alpha}\right) - 1 \approx \frac{T_m - T}{\alpha} \qquad (3)$$

where α = 14 ^{o}C is typical of conditions where natural gas hydrates are found [8].

To use equation (3) to predict the effects of pore geometry on the gas solubility, we need to determine the geometry of the hydrate-liquid surface, as defined by κ and d. Below, we describe how we produce synthetic pore geometries with a simple algorithm that packs together a specified distribution of spherical particles. The key problems to be solved for a given randomly generated point within the porous medium are conceptually simple. 1) Is the point within a pore? 2) What perturbation to the chemical potential would be required to place the point within a pore on the edge of a wetting film? 3) If possible, what perturbation to the chemical potential would be required to place the point within a pore on a constant-curvature hydrate–liquid surface? 4) If possible, what perturbation to the chemical potential would be required to place the point within the largest hydrate crystal that could nucleate within the pore? By finding the smallest chemical potential perturbation that is needed for hydrate–liquid equilibrium at a large number of points, we can effectively determine the solubility perturbation that is required and how this varies with hydrate saturation level. Next, we describe our method for assembling realistic particle packings, and how we predict the methane solubility perturbations that result.

ASSEMBLING A 3-D POROUS MEDIUM

The 3D pore geometry differs from 2D approximations of pore geometries in two important ways. First, there is the fact that the void space itself is three-dimensional and so surfaces within it have two principle radii of curvature rather than just one. Second, there is the difference in geometry that arises from off-plane particle contacts in three-dimensional packing. To develop a realistic, three-dimensional treatment with particles that vary in diameter, we model the pore geometry by simulating the sphere-packing process in Matlab. We designed our program so that we can input any given particle size distribution, as illustrated here by the example shown in Figure 1.

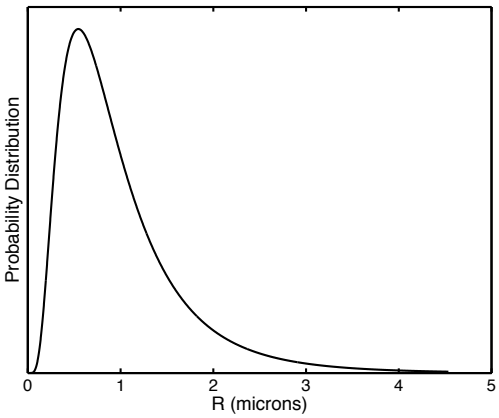

Figure 1. This probability distribution function describes a lognormal particle size distribution. Our sphere-packing algorithm is designed to handle arbitrary distributions that are chosen to match field or laboratory observations.

The probability distribution function is used to create a cumulative distribution function. The cumulative distribution function can be used to create an assortment consisting of any desired number of particles n. The process used to sample the cumulative distribution function is illustrated in Figure 2.

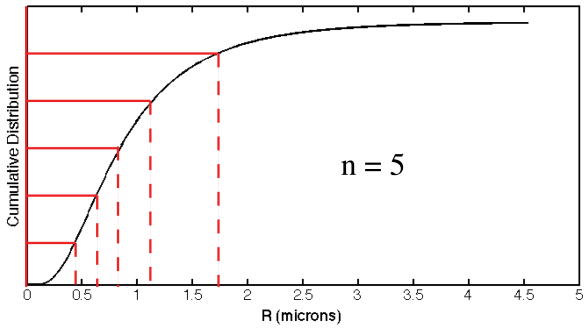

Figure 2. This figure illustrates how a cumulative distribution function can be sampled to create a data set that consists of *n* particles with diverse radii. As shown, n is chosen to equal five so that the divisions are visually accessible. The solid red lines correspond to the divisions of equally spaced probability. The dashed red line links each probability to its corresponding radius.

After we have chosen the desired number of particles *n*, with a distribution of radii that satisfies the given probability distribution function, we randomize the order of the particles. This allows us to then begin the simulation of dropping individual sediment particles, represented by spheres of variable diameter. The spheres go through a sequence of steps to calculate what happens as they are "dropped". We begin by choosing random x and y coordinates down which to drop each sphere from an initial arbitrary height z. If the sphere does not contact another sphere on its way down, it becomes tangent with the floor (Fig. 3a).

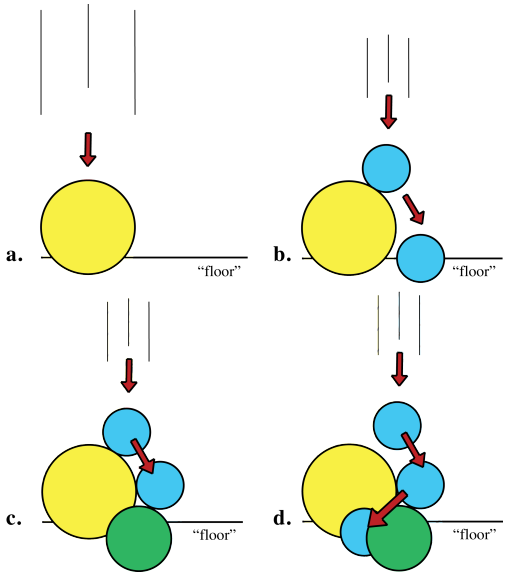

Figure 3. This cartoon simplifies some of the actions that are occurring in the sphere-packing program. (a) The yellow sphere is dropped and does not contact another sphere so it falls to the floor at z = 0. (b) The blue sphere is dropped and first becomes tangent to the yellow sphere; it subsequently rolls to the floor. (c) The blue sphere is dropped and again becomes tangent to the yellow sphere. This time the blue sphere contacts the green sphere on its roll downwards, now the blue sphere is tangent to both the yellow and the green sphere. (d) After the blue sphere becomes tangent to both the yellow and green spheres as in (c), the blue sphere will repeat a number of rotations that allow it to roll downwards while fitting tangentially between the yellow and green spheres.

If the dropped sphere contacts another sphere during its fall, the two spheres become tangent to each other. Next, the dropped sphere begins to tangentially roll down the contacted sphere as can be seen in (Fig. 3b). If the dropped sphere rolls until it has hit the equator of the contacted sphere, it is dropped again and the process is repeated. If the dropped sphere makes contact with the floor it stops. If the dropped sphere makes contact with a second sphere it then tries to "fit" itself between the two spheres (Fig. 3c – d).

The fitting process involves multiple steps. The dropped sphere rotates laterally away from the second sphere that it has contacted, then the dropped sphere rolls downward longitudinally until it contacts the second sphere again and this process continues to repeat itself. The movement of the dropped sphere stops if it contacts i) a third sphere, ii) the floor, or iii) it has reached a specified maximum number of rotations. The result of this process is a synthetic three-dimensional porous medium, like that illustrated in Figure 4.

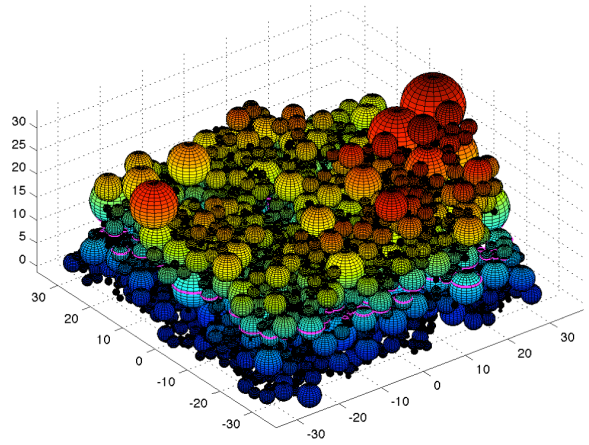

Figure 4. An example packing of heterogeneously sized spheres. The pink lines show the location of the plane that defines the cross section shown in Figure 5.

As an initial step in developing our solubility calculations and testing the particle-packing algorithm, we select cross-sections through our synthetic porous media, such as that shown by the pink lines midway up in Figure 4. The spheres sampled in this way are shown in Figure 5. Calculations of porosity compare favorably against known behavior of random close-packed uniform spheres, and give reasonable results for more realistic polydispersed media. Two-dimensional treatments of solubility perturbations will next be applied to the synthetic cross sections from our three-dimensional packing codes. These are expected to do a faithful job at predicting the influence of wetting interactions on solubility. However, the validity of the resulting approximation for surface energy effects is less certain since the surface curvature normal to the cross section is not properly accounted for and could vary between arbitrarily large negative and positive values. The two-dimensional approximation effectively amounts to setting this second principle radius of curvature to equal to the first, which we expect to act as a reasonable compromise between these limits. The testing of

these ideas awaits the full three-dimensional calculations that are currently under development.

SURFACE AND WETTING EFFECTS

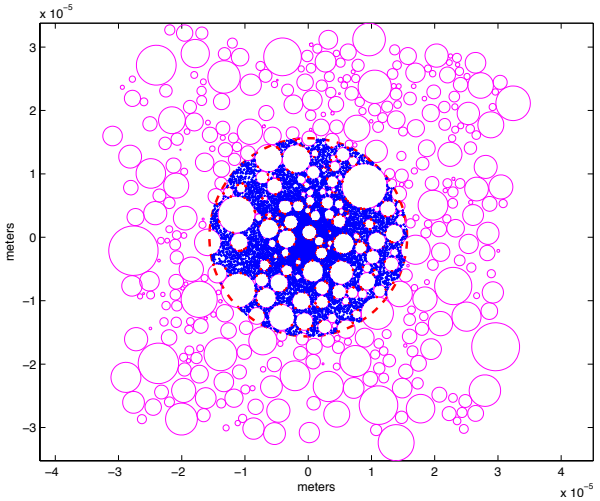

Figure 5. A cross section taken from the sphere packing shown in Figure 4. Pink circles represent the solid particles. Blue crosses show points where residual liquid remains until the hydrate-liquid interface can overcome curvature effects. Red crosses show locations where liquid remains in a thin film surrounding a particle until the undercooling increases sufficiently. The test region shown includes 20,000 test points.

A cross-section (Fig. 5a) is chosen from the 3-D packing of spheres (Fig. 4) and the resulting circular intersections are used to approximate representative pore geometries. We next choose a large number of test points that are randomly distributed within a test area that contains a large number of particles and pores within the chosen plane. The porosity is determined simply as the fraction of the points that land outside of all the model particles within the test region. The more challenging problem is to use similar Monte Carlo integration techniques to calculate the undercooling required for hydrate to form at each of these test points.

For each test point that does not land within a solid particle, we seek the minimum undercooling from Eq. 1 required for hydrate to form. First, we calculate the distance d to the nearest particle to determine the undercooling that would be required for the point to be at the edge of a premelted film, which satisfies

$$T_m - T \approx \frac{T_m}{\rho_h L}\left[P_0 \left(\frac{\lambda}{d} \right)^{\beta} - \frac{2\gamma_{hl}}{R} \right], \qquad (4)$$

where $\kappa = -2/R$ is the curvature along the surface of the nearest particle. The geometry of the pore space may allow for hydrate to form before this undercooling is achieved if the test point is far enough from all particle surfaces for curvature effects to determine the perturbation to the phase behavior (i.e. $d \gg \lambda$). Two different cases are examined: i) the undercooling that would be necessary to place the test point on the surface of the largest sphere that would fit within the pore space; ii) the undercooling that would be necessary to place the point within the largest sphere that would fit within the pore space. Each of these curvature-controlled undercoolings satisfies

$$T_m - T \approx \frac{T_m}{\rho_g L}\frac{2\gamma_{hl}}{R_h}, \qquad (5)$$

where R_h will be the same for both cases when the test point is close to a constriction between particles, but only case ii) will be compatible with the geometrical constraints when the test point is close to the center of a pore. As noted above, the undercooling approximated by equation (5) does not account for the off-plane geometry that may cause the second principle radius of curvature to be significantly larger or smaller than R_h. The approximate treatment explored here will be tested further in future work.

By determining the minimum value of $T_m - T$ from equations (4) and (5) at each of the test points, we can effectively determine how the residual liquid saturation (i.e. one minus the hydrate saturation) changes with undercooling. At any particular undercooling, we simply compare the fraction of the test points that remain within the liquid to the total number of test points within the pores of the test region. Figure 6 shows how the liquid saturation level changes with undercooling in the example packing illustrated in Figures 4 and 5. The dominant effect that allows methane to stay in solution beyond the bulk equilibrium temperature of hydrate changes with the amount of residual liquid saturation. Close to the bulk equilibrium temperature, curvature effects are responsible for the majority of the residual liquid. In the example

shown in Figure 6, curvature effects dominate the perturbations to the phase behavior until hydrate fills almost 90% of the pore space. As the temperature continues to cool, premelted films are responsible for an increasing proportion of the remaining liquid. This is consistent with findings for two-dimensional packings, however, two-dimensional particle packings underestimate the amount of pore space by creating an unrealistic degree of tangency between the circles in cross-section. Further efforts to account for the influence of off-plane obstructions on the value of the mean curvature R_h in equation (4) are ongoing.

INFLUENCE OF SALT

Many methane hydrate deposits are found along continental margins in ocean sediments. Salt is excluded from the hydrate structure as it forms, and colligative effects can become important for altering methane solubility (Fig. 6b). Assuming a linear liquidus, the local bulk equilibrium temperature T_m is related to the bulk equilibrium temperature of the pure system by

$$T_m \approx T_{m0} - \Gamma c. \qquad (6)$$

If the pore space contains salt with bulk concentration c_B and the salt is completely excluded from the hydrate structure, then its dissolved concentration in the residual liquid is simply

$$c \approx \frac{c_B}{S_l}. \qquad (7)$$

Together, Eqs. (6) and (7) imply that the local bulk equilibrium temperature can be written as

$$T_m \approx T_{m0} - \Gamma \frac{c_B}{S_l}. \qquad (8)$$

Since wetting interactions and surface energy effects continue to perturb the chemical potential, as described by Eq. (1), we have already performed the calculations necessary to evaluate how the hydrate and liquid saturations change in our model pore space. Assigning a constant value for c_B, Figure 6b) shows how liquid saturation varies with the absolute undercooling, defined as the difference between the bulk equilibrium temperature for the salt-free system T_{m0} and the local temperature T. As liquid saturation falls, increases to the local solute concentration c cause the saturation dependence on absolute undercooling to change. However, we should note that these simple calculations do not account for any affects that solute concentration might have on the strength or nature of the wetting interactions themselves.

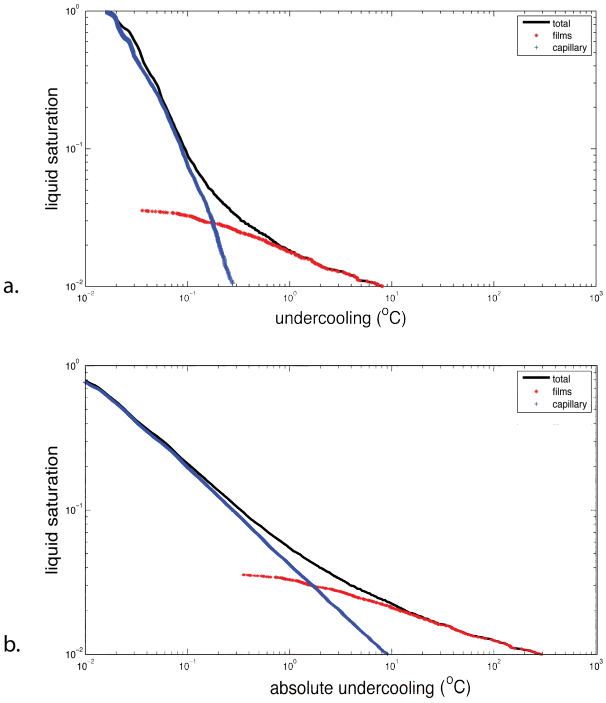

Figure 6. Illustrates the liquid fraction of water as it cools below the bulk freezing temperature using 20,000 test points. The blue lines represent the liquid fraction induced by pore space geometry. The red lines represent the liquid fraction that remains due to the thin premelted films on the surface of particles. The thin black lines represent the total remaining liquid fraction as the temperature continues to drop. First we consider methane as the only solvent in the water (a). Then colligative effects are added to simulate the impurities of ocean water in sediment (b). Notice that for both cases a power-law approximation of liquid saturation with respect to undercooling becomes less valid after the wetting interactions become dominant.

SUMMARY

We have developed a tool for packing a heterogeneous medium that is capable of using input particle-size distributions from field-collected data. This tool will improve our understanding of the specific geometries and locations of hydrate precipitation in nature.

Although the surface curvature effects on hydrate precipitation within the pore space differ between two- and three-dimensional cases, we suspect that positive and negative curvatures in the direction perpendicular to a particular cross-section may tend to largely cancel and we plan to test this hypothesis as we continue with model development.

We can use our packing-tool to create particle size distributions from field-collected data. Once our solubility parameterizations have been developed and tested, they will be used in models to predict the development of hydrate anomalies in synthetic deposits chosen to match characteristics at known hydrate-bearing localities.

ACKNOWLEDGEMENTS
This work is supported by the U.S. Department of Energy under agreement DE-FE0013565.

REFERENCES
[1] Sloan ED. Fundamental principles and applications of natural gas hydrates. Nature 2003; 426:353-363.
[2] Sultan N, Cochonat P, Foucher JP, and Mienert J. Effect of gas hydrates melting on seafloor slope instability. Marine Geology 2004; 213(1):379–401. (slope instability)
[3] Boswell R, Collett, TS. Current perspectives on gas hydrate resources. Energy Environ. Sci. 2011; 4:1206-1215.
[4] Dickens GR, O'Neil JR, Rea DK, Owen RM. Dissociation of oceanic methane hydrate as a cause of the carbon isotope excursion at the end of the Paleocene. Paleoceanography 1995; 10(6):965-971.
[5] Wallmann K, Pinero E, Burwicz E, Haeckel M, Hensen C, Dale A, and Ruepke L. The Global Inventory of Methane Hydrate in Marine Sediments: A Theoretical Approach. Energies 2012: 5(7):2449-2498
[6] Andersland OB, and Ladanyi B. *Frozen* New York: John Wiley and Sons Inc., 2004.
[7] Rempel AW. A model for the diffusive growth of hydrate saturation anomalies in layered sediments. Journal of Geophysical Research: Solid Earth 2011; 116(B10):1978-2012.
[8] Davie MK, Zatsepina OY, Buffett BA. *Methane solubility in marine hydrate environments*, Marine Geol. 2004; 203: 177-184.